# First-Principles Theory of the Relativistic Magnetic Reconnection Rate in Astrophysical Pair Plasmas

Matthew Goodbred and Yi-Hsin Liu
*Dartmouth College, Hanover, New Hampshire 03755, USA*

(Received 16 August 2022; revised 16 October 2022; accepted 15 November 2022; published 20 December 2022)

We develop a first-principles model for the relativistic magnetic reconnection rate in strongly magnetized pair plasmas. By considering the energy budget and required current density near the x-line, we analytically show that in the magnetically dominated relativistic regime, the x-line thermal pressure is significantly lower than the upstream magnetic pressure due to the extreme energy needed to sustain the current density, consistent with kinetic simulations. This causes the upstream magnetic field lines to collapse in, producing the open outflow geometry which enables fast reconnection. The result is important for understanding a wide range of extreme astrophysical environments, where fast reconnection has been evoked to explain observations such as transient flares and nonthermal particle signatures.

DOI: 10.1103/PhysRevLett.129.265101

*Introduction.*—Magnetic reconnection is a fundamental plasma phenomenon which explosively converts magnetic energy into plasma energy. Inflowing plasma carries magnetic flux into the diffusion region. There plasma is energized and ejected around the *x-line* into the exhaust (see Fig. 1). Reconnection is thought to play a critical role in ubiquitous astrophysical environments where the magnetic field energy density can exceed the rest mass energy density of the ambient plasma [1], characterized by the asymptotic magnetization parameter $\sigma_0 \equiv B_{x0}^2/4\pi n_0 mc^2$. Here, $B_{x0}$ and $n_0$ are the asymptotic (background) reconnection magnetic field strength and particle density, respectively. When $\sigma_0 \gg 1$, relativistic effects become important. The reconnection rate is the most important characteristic of magnetic reconnection since it describes how fast reconnection processes magnetic flux and indicates the particle acceleration timescale. Fast reconnection, on the order of $R_0 \sim 0.1$ in normalized units, has been evoked to explain transient gamma-ray flares in active galactic nuclei (AGNs) [2,3], the dissipation of magnetic "hair" in black hole (BH) magnetospheres [4], BH accretion disk coronal heating and flares [5], gamma-ray bursts in pulsar nebula [6,7], the rapid dissipation of Poynting flux in pulsar winds [8,9], and giant magnetar flares [10]. Electron-positron (pair) plasmas are thought to dominate the plasma environment of pulsar winds [11] and play a significant role in BH magnetospheres, including AGN/BH jets [12,13]. Highly magnetized electron-ion plasmas may be relevant in BH accretion discs [5] and tera-electron-volt flares in relativistic AGN jets [2,14]. In these contexts, reconnection can accelerate particles to ultrarelativistic energies and produce broad nonthermal spectra [15–18]. Despite the great interest in pair and relativistic electron-ion reconnection to explain numerous puzzling observations in astrophysics, there is yet no first-principles theory for the rate of reconnection in these astrophysical plasmas [1].

It was recently shown that in nonrelativistic ($\sigma_0 \ll 1$) electron-ion plasmas, reconnection is fast because Hall electromagnetic fields divert inflowing Poynting flux around the x-line. Electrons remain frozen-in within the ion diffusion region, and as the primary out-of-plane current carrier, they drag reconnecting magnetic field lines into the out-of-plane Hall quadrupole magnetic field. Inflowing electrons are subsequently deflected by this Hall magnetic field into the outflow direction, carrying the magnetic energy away from the x-line. The resulting energy void prevents thermal pressure build-up at the x-line, and upstream magnetic field lines bend in to maintain force balance along the inflow [19]. This creates the open outflow geometry necessary for fast reconnection [20]. The x-line pressure depletion is also observed during fast reconnection in relativistic pair plasmas [21]. However, the cause of this depletion must be drastically different since the plasma species' equal mass eliminates the Hall effect, and all inflowing magnetic energy can be transferred to the plasma at the x-line. Similarly, in the large $\sigma$ limit of electron-ion reconnection, the scale separation between species may be less relevant since the effective relativistic masses of electrons and ions become equivalent, indicating that relativistic electron-ion reconnection behaves similarly to pair plasma reconnection where the Hall effect is absent [22].

In this Letter, we identify an entirely different mechanism leading to fast reconnection in relativistic pair plasmas. We show that in the magnetically dominated relativistic regime, the x-line thermal pressure cannot balance the upstream magnetic pressure due to the energy needed to sustain the extreme current density. The

 

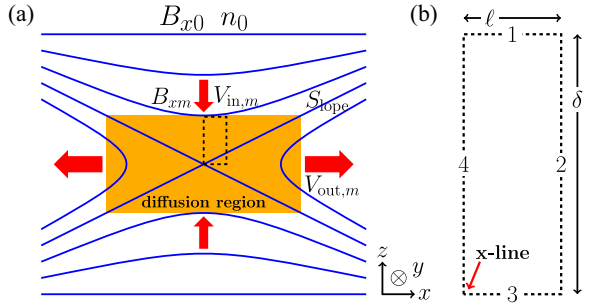


FIG. 1. Panel (a) depicts the reconnection geometry, including the distinction between asymptotic and microscale quantities. Panel (b) is an enlargement of the dotted box in panel (a), the Gaussian surface to the upper right of the x-line.

implosion of the upstream magnetic pressure into the x-line triggers fast reconnection. With this insight, we develop a first-principles model for the reconnection rate in strongly magnetized pair plasmas with a simple magnetic field reversal. The model predictions compare well to fully kinetic particle-in-cell (PIC) simulations.

*Theory.*—Our model of the x-line plasma pressure considers two basic properties of pair plasma reconnection: the energy budget around the x-line and the current density necessary for the field reversal. As in Liu *et al.* [19], these properties are analyzed within a Gaussian surface with the bottom-left corner at the x-line, illustrated by the dotted rectangle in Fig. 1. The surface extends to the current sheet half-thickness $\delta$ in the $z$ direction and has small width $\ell \ll \delta$ in the $x$ direction, as shown in Fig. 1(b). The inflow, outflow, and out-of-plane directions are $z$, $x$, and $y$, respectively. The asymptotic background conditions of magnetic reconnection can be very different from the microscale conditions at the edge of the diffusion region, as illustrated in Fig. 1(a) [20]. Thus, asymptotic and microscale quantities are denoted with "0" and "$m$" subscripts, respectively. We will also refer to local quantities around the diffusion region by the labeled surfaces in Fig. 1(b). Note that surface 1 is at the microscale. Electron and positron species are specified by $(-)$ and $(+)$ subscripts, but due to the symmetry between species, we omit subscripts unless relevant.

Quantities in the proper frame of a species are primed. Roman letters index the three-dimensional Euclidean space ($i = x, y, z$). Greek letters index the four-dimensional flat space-time ($\alpha = 0, x, y, z$), and we use the mostly positive metric tensor $\eta^{\alpha\beta} = \mathrm{diag}(-1, 1, 1, 1)$. The speed of light $c = 1$, but we write the unit where instructive. In the following analysis, we follow the tensor formalism of Zenitani [23]. The stress-energy (SE) tensor is obtained from the particle four-velocity $u^\alpha = (\gamma, \gamma\mathbf{v})$ and Lorentz factor $\gamma = 1/[1 - v^2]^{1/2}$ as

$$T^{\alpha\beta} = m \int f(\mathbf{u}) u^\alpha u^\beta \frac{d^3u}{\gamma}, \tag{1}$$

which is a four tensor because it is a linear combination of the dyadic four-tensor $u^\alpha u^\beta$ and since the distribution function $f(\mathbf{u})$ and $d^3u/\gamma$ are both Lorentz invariant. The normalization of $f(\mathbf{u})$ is defined by $\int f(u) d^3u = n$. Although generally not explicitly denoted, $f(\mathbf{u})$ is also a function of location.

For the remainder of this Letter, all velocities refer to the Eckart velocity. The Eckart four-velocity $U_E^\alpha \equiv N^\alpha/n'$ where $N^\alpha \equiv \int f(\mathbf{u}) u^\alpha (d^3u/\gamma)$ is the particle number flux four vector and $n' = (-N^\alpha N_\alpha)^{1/2}$ is the proper density [24]. In the Eckart frame, the spatial components $U_E^i = 0$, and thus the spatial components of the particle number flux four vector vanish (i.e., $N^i = 0$), indicating the rest frame of the bulk fluid. Similarly, the Eckart three-velocity $V_E^i \equiv U_E^i/\Gamma_E$ with $\Gamma_E \equiv 1/[1 - V_E^2]^{1/2}$ the Lorentz factor of the Eckart frame. Hereafter, we set $U^\alpha = U_E^\alpha$ and $V^i = V_E^i$.

With this background, the relativistic electron Ohm's law is written as

$$\mathbf{E} + \mathbf{V} \times \mathbf{B} = -\frac{1}{\Gamma e n'} [\partial_j (\mathcal{E} U^i U^j + Q^{ij} + P^{ij}) + \partial_t T^{i0}], \tag{2}$$

where $Q^{ij}$ is the heat flux tensor and $P^{ij}$ is the pressure tensor [23]. See the Appendix A for the full derivation. It is known that in the relativistic regime, the bulk inertia term of Ohm's law balances the reconnection electric field $E_y$ at the edge of the diffusion region [23,25,26], as seen by comparing the blue to the red curve in Fig. 2(a). In Appendix A, we evaluate Eq. (2) at the transition region close to surface 1 and find that the current sheet width is approximately the pair plasma inertial length based on the proper density inside the current sheet:

$$\delta \approx \sqrt{\frac{mc^2}{8\pi n_3' e^2}}. \tag{3}$$

This prediction is validated in Fig. 2(a) and has been noted in previous works [11,27]. Close to the x-line, the relativistic compression of the plasma in the current sheet is based on the Lorentz factor of the bulk flow in the $y$ direction, $\Gamma_y \equiv 1/[1 - V_{y3}^2]^{1/2}$, so that Ampère's law is $B_{xm}/4\pi\delta = 2 e n_3' \Gamma_y V_{y3}$. Plugging in Eq. (3), we solve for

$$\Gamma_y \approx \sqrt{1 + \frac{\sigma_m}{2}\left(\frac{n_1}{n_3'}\right)}, \tag{4}$$

where $\sigma_m = B_{xm}^2/4\pi n_1 mc^2$ is the microscale magnetization parameter.

Next, we consider the energy available to support the x-line plasma pressure. The energy conservation equation is obtained from the vanishing four divergence of the time component of the total SE tensor:

$$\partial_\alpha (T^{0\alpha}_{(+)} + T^{0\alpha}_{(-)} + T^{0\alpha}_{\mathrm{EM}}) = 0, \tag{5}$$

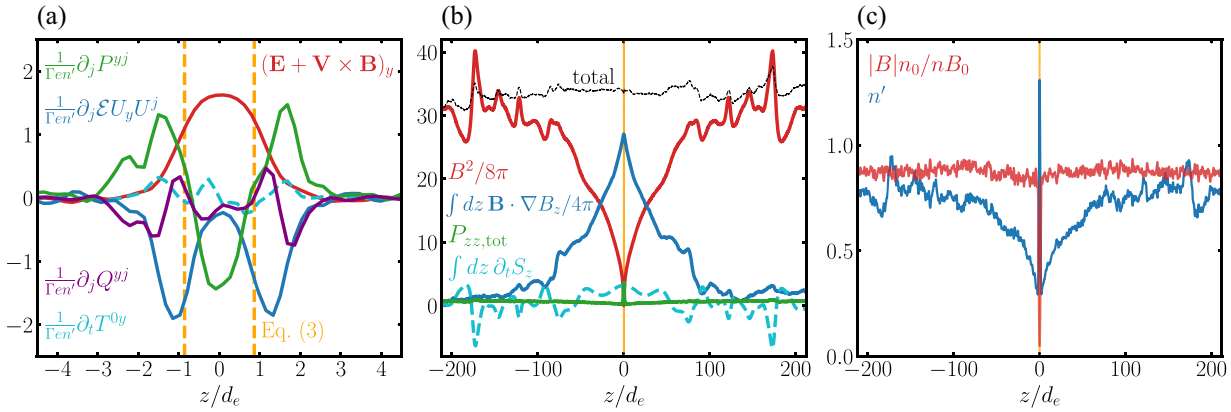


FIG. 2. Panel (a) shows the out-of-plane electron Ohm's law around the x-line. Panel (b) plots the total pressure balance including both species along the inflow symmetry line, demonstrating that $P_{zz}|_{\mathrm{xline}} \ll B_{x0}^2/8\pi$. The Poynting flux time derivative balances fluctuations far upstream. Panel (c) shows the electron proper density $n'$ and the normalized $|B|/n$ ratio along the inflow symmetry line. Orange vertical bars show the prediction of the diffusion region thickness based on Eq. (3). All plots are from the $\sigma_{0,\mathrm{init}} = 100$ simulation run at $t = 379/\omega_p$, but similar features are observed in all runs.

where $T^{\alpha\beta}_{\mathrm{EM}} = (1/4\pi)[F^{\alpha\mu}F^{\beta}_{\mu} - \eta^{\alpha\beta}F_{\mu\nu}F^{\mu\nu}/4]$ is the electromagnetic SE tensor. We wish to analyze this equation within the Gaussian surface indicated by the dotted box Fig. 1. By symmetry around the x-line, the energy fluxes through surfaces 3 and 4 vanish. In steady state $\partial_t = 0$, so we use the divergence theorem to rewrite Eq. (5) as

$$\int_1 (T^{0z}_{(+)} + T^{0z}_{(-)} + T^{0z}_{\mathrm{EM}})dx + \int_2 (T^{0x}_{(+)} + T^{0x}_{(-)} + T^{0x}_{\mathrm{EM}})dz = 0. \tag{6}$$

With a cold upstream plasma, $\gamma \simeq 1$ in the inflow region. Thus, by Eq. (1),

$$(T^{0z}_{(+)} + T^{0z}_{(-)})\big|_1 \approx 2n_1 mc^2 V_{z1}. \tag{7}$$

In this Letter we aim to analytically show that $P_{zz}|_{\mathrm{xline}}$ (i.e., a thermal spread in $v_z$) is significantly lower than the asymptotic magnetic pressure in the large-$\sigma_0$ limit [as in the comparison of the green and red curves in Fig. 2(b)] because the current carrier bulk flow kinetic energy takes most of the incoming magnetic energy. While there is in reality some thermal spread, for the purposes of this model we assume the plasma is cold in the $v_y$ and $v_x$ directions, which minimizes the energy required to sustain the current. Since $d^3u = \gamma^5 d^3v$, we consider the distribution function $g \equiv \gamma^5 f = F(v_z)\delta(v_x - V_x)\delta(v_y - V_y)$, so that $g$ is the number density in three-velocity phase space. Then

$$\begin{aligned}(T^{0x}_{(+)} + T^{0x}_{(-)})\big|_2 &\approx 2m\int f_2 u_x c d^3u = 2m\int g_2 \gamma v_x c d^3v \\ &= 2mV_{x2}c\int F_2(v_z)\gamma(v_z)dv_z \\ &= 2\langle\gamma(v_z)\rangle_2 n_2 mc^2 V_{x2},\end{aligned} \tag{8}$$

where we define $\gamma(v_z) \equiv \gamma(v_x = V_x, v_y = V_y, v_z)$ and the ensemble average $\langle A\rangle \equiv \int gAd^3v/\int gd^3v$. Last, the inflowing electromagnetic energy flux $T^{0z}_{\mathrm{EM}}|_1 = -E_y B_{xm}/4\pi$. The plasma is frozen-in in the upstream, so $E_y = -V_{z1}B_{xm}$. The result is

$$T^{0z}_{\mathrm{EM}}|_1 = \frac{B_{xm}^2}{4\pi}V_{z1}. \tag{9}$$

In the $|\partial_x B_z| \ll |\partial_z B_x|$ limit, we can ignore the outflowing EM energy flux: $T^{0x}_{\mathrm{EM}}|_2 \approx 0$. Combining Eqs. (7)–(9) with Eq. (6), we obtain

$$\left[2n_1 mc^2 + \frac{B_{xm}^2}{4\pi}\right]V_{z1}\ell + 2\langle\gamma(v_z)\rangle_2 n_2 mc^2 V_{x2}\delta \approx 0. \tag{10}$$

With the particle number continuity equation $n_1 V_{z1}\ell + n_2 V_{x2}\delta = 0$, we solve Eq. (10) for

$$\langle\gamma(v_z)\rangle_2 \approx 1 + \frac{\sigma_m}{2}. \tag{11}$$

Finally, we can estimate the x-line pressure. At the midplane $V_z = 0$, so the total $P_{zz}$ at surface 3 is given by

$$\begin{aligned}(T^{zz}_{(+)} + T^{zz}_{(-)})\big|_3 &= 2m\int f_3 \frac{u_z^2}{\gamma}d^3u = 2m\int g_3 \gamma v_z^2 d^3v \\ &= 2mc^2\int F_3\gamma(v_z)[1 - V_{x3}^2 - V_{y3}^2 - 1/\gamma(v_z)^2]dv_z \\ &= 2n_3 mc^2\left[\frac{\langle\gamma(v_z)\rangle_3}{\Gamma_y^2} - \left\langle\frac{1}{\gamma(v_z)}\right\rangle_3\right],\end{aligned} \tag{12}$$

where we used the fact that $V_{x3} \to 0$ in the $\ell \to 0$ limit. Using the inequality $\langle 1/A\rangle \geq 1/\langle A\rangle$ for $A > 0$ and $n_3 = \Gamma_y n_3'$, we then arrive at

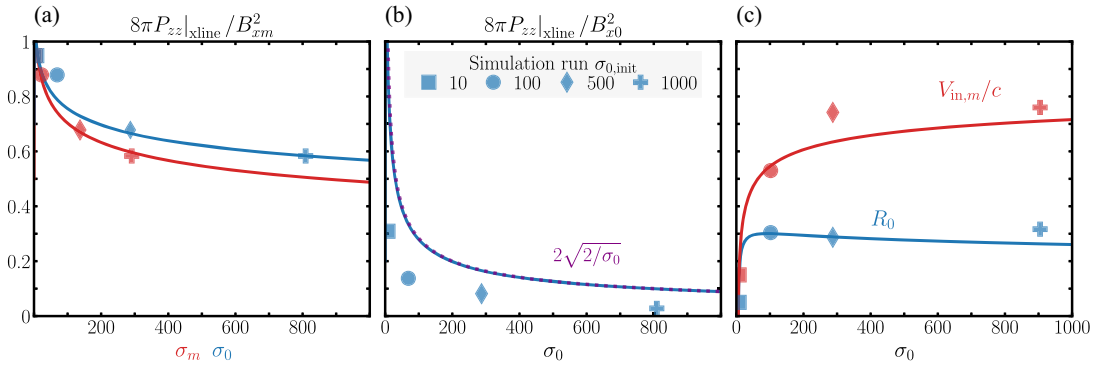


FIG. 3. Panel (a) shows the microscale x-line pressure ratio as a function of both $\sigma_m$ and $\sigma_0$. Panel (b) shows the pressure ratio relative to the asymptotic magnetic pressure as a function of $\sigma_0$. The dashed purple curve is the $\sigma_0 \gg 1$ limit of the numerical solution, $2\sqrt{2/\sigma_0}$. Panel (c) shows the reconnection rate $R_0$ and the microscopic inflow speed $V_{{\rm in},m}/c \simeq E_y/B_{xm}$ as a function of $\sigma_0$. To measure $R_0$ from simulations, we use $E_y = \partial_t[\max(A_y) - \min(A_y)]$ where $A_y$ is the $y$ component of the vector potential along the midplane. Predictions of the model are solid curves numerically calculated with Eqs. (14)–(16), and (18). Markers are direct measurements of the respective quantities from simulations shortly after the reconnection rate peaks.

$$P_{zz}|_{\rm xline} \le 2n_3' mc^2 \left[\frac{\langle\gamma(v_z)\rangle_3}{\Gamma_y} - \frac{\Gamma_y}{\langle\gamma(v_z)\rangle_3}\right]. \tag{13}$$

Equation (13) makes clear the factors affecting the x-line thermal pressure. $\langle\gamma(v_z)\rangle_3$ is controlled by the energy per particle that includes thermal motions in $v_z$. $\Gamma_y$ is purely controlled by the current carrier bulk flow. If all available energy is used to drive the current, then $\Gamma_y \simeq \langle\gamma(v_z)\rangle_3$, and $P_{zz}|_{\rm xline}$ becomes very small. Conversely, if only a small fraction of the total energy is needed to drive the current, $P_{zz}|_{\rm xline}$ can become significant. Approximating $\langle\gamma(v_z)\rangle_3 \approx \langle\gamma(v_z)\rangle_2$ in the $\ell \to 0$ limit, we substitute Eq. (11) for $\langle\gamma(v_z)\rangle_3$ and Eq. (4) for $\Gamma_y$ to solve for the x-line pressure ratio:

$$\frac{8\pi P_{zz}|_{\rm xline}}{B_{xm}^2} \le 2\frac{[2+(\sigma_m/2)](n_3'/n_1) - 1}{[1+(\sigma_m/2)]\sqrt{1+(\sigma_m/2)(n_1/n_3')}}. \tag{14}$$

The only free parameter in Eq. (14) is the proper compression ratio $n_3'/n_1$. To determine this ratio, we first observe in simulations that the proper density around the x-line matches the inflow asymptotic density: $n_3' \approx n_0$. Second, the upstream magnetic flux tube expands close to the diffusion region as the exhaust opens. The cold upstream plasma does not quickly redistribute itself along the expanding field lines. Thus, local conservation of mass content within flux tubes implies that $n_0/n_1 \approx B_{x0}/B_{xm}$ [28–30]. These two features are justified in Fig. 2(c). It follows that

$$n_3'/n_1 \approx B_{x0}/B_{xm}. \tag{15}$$

In the cold upstream plasma limit where $P_{zz}|_{\rm xline} \approx P_{zz}|_\delta^0$, we close Eq. (14) using the following relations which were derived in Liu *et al.* [19,20] based on the force balance along the inflow symmetry line and the assumption that separatrix field lines have the same slope, $S_{\rm lope}$ [see Fig. 1(a)], inside and outside the diffusion region:

$$S_{\rm lope}^2 \approx 1 - \frac{8\pi P_{zz}|_{\rm xline}}{B_{xm}^2} \tag{16a}$$

$$\frac{B_{xm}}{B_{x0}} \approx \frac{1 - S_{\rm lope}^2}{1 + S_{\rm lope}^2}. \tag{16b}$$

*Results.*—Using Eqs. (14)–(16) we numerically solve for the microscale and asymptotic x-line pressure ratios as a function of $\sigma_m$ or $\sigma_0$. Note that the relation between $\sigma_m$ and $\sigma_0$ is obtained numerically from the same equations. The results are shown in Fig. 3, where we compare the theoretical predictions (solid curves) to a series of four 2.5D pair plasma PIC simulations (markers) with different initial magnetizations $\sigma_{0,\rm init}$. Figures 3(a) and 3(b) show excellent agreement between the simulation x-line pressure ratios and the predicted scaling relation with both $\sigma_m$ and $\sigma_0$. In Fig. 3(b), we find a simple scaling of $8\pi P_{zz}|_{\rm xline}/B_{x0}^2 \sim 2\sqrt{2/\sigma_0}$ in the $\sigma_0 \gg 1$ limit (dashed curve). Note that fast reconnection is realized as long as $8\pi P_{zz}|_{\rm xline}/B_{x0}^2 < 1$ [21].

We can also predict the reconnection rate from the x-line pressure ratio. The reconnection rate normalized to the asymptotic magnetic field is defined as $R_0 \equiv cE_y/B_{x0}V_{A0}$, where $V_{A0}$ is the asymptotic upstream Alfvén speed. This can be written as

$$R_0 \simeq \left(\frac{B_{zm}}{B_{xm}}\right)\left(\frac{B_{xm}}{B_{x0}}\right)\left(\frac{V_{{\rm out},m}}{V_{A0}}\right), \tag{17}$$

where $V_{\mathrm{out},m}$ is the outflow speed at the edge of the diffusion region. When $\sigma_m \gg 1$, $V_{\mathrm{out},m} \sim V_{A0} \sim c$ [31], and using $B_{zm}/B_{xm} \approx S_{\mathrm{lope}}$ we can solve for the reconnection rate

$$R_0 \simeq S_{\mathrm{lope}}\left(\frac{1-S_{\mathrm{lope}}^2}{1+S_{\mathrm{lope}}^2}\right), \tag{18}$$

where $S_{\mathrm{lope}}$ is calculated using Eqs. (16a) and (14), (15). From Fig. 3(c), the model predicts a slower reconnection rate $R_0 \sim \mathcal{O}(0.01)$ for $\sigma_0 \sim \mathcal{O}(1)$, which rapidly increases to $R_0 \sim 0.1$–$0.3$ for $\sigma_0 \gtrsim 10$. The prediction yields excellent agreement with our simulations and previously observed scaling [17].

*Conclusions.*—We have shown that in relativistic pair plasma reconnection, the x-line plasma pressure cannot balance the upstream magnetic pressure given the need to maintain the extreme x-line current density. In the absence of the Hall effect, essentially all inflowing electromagnetic energy near the x-line can be locally converted to plasma energy. However, current carriers constantly turn into the outflow. The energetic requirement to replenish these current carriers becomes significant at high $\sigma$ since the Lorentz factor associated with the current $\Gamma_y$ becomes extremely large. Therefore, only a small fraction of electromagnetic energy is available to maintain the x-line pressure $P_{zz}|_{\mathrm{xline}}$, making it significantly lower than the asymptotic upstream magnetic pressure $B_{x0}^2/8\pi$, leading to fast reconnection. We derived a simple scaling relation $8\pi P_{zz}|_{\mathrm{xline}}/B_{x0}^2 \sim 2\sqrt{2/\sigma_0}$ in the $\sigma_0 \gg 1$ limit. The predicted reconnection rates agree well with PIC simulations.

While the reconnection outflow geometry opens out due to x-line pressure depletion in both astrophysical plasmas and nonrelativistic electron-ion plasmas, the exhaust dynamics can be different. In the latter, the exhaust pressure can build up because Hall electromagnetic fields divert energy to the outflow region, and the energy required for the primary current carrier (electrons) is negligible [19]. This results in a single, stable x-line. In contrast, pair plasma reconnection lacks the diversion of energy flow by Hall fields, and the relativistic current carriers take significant energy, causing low pressure within exhausts as well. Thus, the current layer can collapse even in the "once opened" exhaust region, explaining the bursty nature that recursively triggers and ejects magnetic islands [21]. This time dependency, however, is not the driver and does not affect the average reconnection rate in collisionless plasmas. In comparison, the current in relativistic magnetohydrodynamics models requires no energy, and the plasmoid instability was invoked to explain the fast rate [32,33].

More work is needed to understand how this model couples with theories of turbulent driving and onset. While magnetohydrodynamics-scale turbulence may enable fast reconnection to proceed independently of kinetic physics in the current sheet [34], some evidence shows that kinetic ($d_e$-scale) reconnecting layers persist and dominate a current sheet that is filled with external and self-generated turbulence [35]. Moreover, kinetic effects may enhance reconnection rates in the presence of broadband turbulence [36]. In these cases, turbulent driving may lead to fast reconnection on kinetic scales, as detailed in this Letter. A resolution to this complex interplay requires separate dedicated efforts.

In summary, our model provides the critical theoretical foundation for fast reconnection in collisionless astrophysical plasmas. We expect these fundamental considerations of the current-carrier requirement and x-line energy budget to carry over to three-dimensional (3D) systems.

M. G. is thankful for support from the Wilder Fellowship at Dartmouth College and NSF Grant No. PHY-1902867. Y. L. is grateful for support from NSF Grant No. PHY-1902867 through the NSF/DOE Partnership in Basic Plasma Science and Engineering, NSF Career Award No. 2142430 and NASA's MMS mission 80NSSC21K2048. We thank Xiaocan Li for helpful discussions and assistance with simulations. Simulations were performed at the National Energy Research Scientific Computing Center at LBNL.

*Appendix A: Derivation of the relativistic Ohm's law and the diffusion region width.*—The following derivation of the relativistic Ohm's law is due to Zenitani [23]. The stress-energy tensor can be decomposed as

$$T^{\alpha\beta} = \mathcal{E}U^\alpha U^\beta + Q^{\alpha\beta} + P^{\alpha\beta}, \tag{A1}$$

where $U^\alpha$ is an arbitrary flow four velocity. With $\Delta^{\alpha\beta} \equiv \eta^{\alpha\beta} + U^\alpha U^\beta$ as the projection tensor, $\mathcal{E} \equiv T^{\alpha\beta}U_\alpha U_\beta$ is the energy density in the $U^\alpha$-moving frame. $Q^{\alpha\beta} = q^\alpha U^\beta + U^\alpha q^\beta$ is the heat flux tensor, where $q^\alpha \equiv -\Delta^\alpha_\beta T^{\beta\mu}U_\mu$ is the heat flux four vector. $P^{\alpha\beta} \equiv \Delta^\alpha_\mu \Delta^\beta_\nu T^{\mu\nu}$ is the pressure tensor projected in the $U^\alpha$-moving frame.

With $U^\alpha = U^\alpha_E$ (the Eckart four velocity), the energy-momentum equation for the electron species is then given by

$$\partial_\beta T^{\alpha\beta}_{(-)} = -en' F^{\alpha\beta}U_\beta, \tag{A2}$$

where $F^{\alpha\beta}$ is the electromagnetic tensor. The relativistic electron Ohm's law is obtained from the space components of Eq. (A2):

$$\mathbf{E} + \mathbf{V}\times\mathbf{B} = -\frac{1}{\Gamma en'}[\partial_j(\mathcal{E}U^iU^j + Q^{ij} + P^{ij}) + \partial_t T^{i0}]. \tag{A3}$$

Here, $\mathbf{V}$ is the electron Eckart three velocity, and $\Gamma$ is the Lorentz factor of the Eckart frame.

As discussed the main text, it is known that in the relativistic regime, the bulk inertia term of the Ohm's law balances the reconnection electric field $E_y$ at the edge of the diffusion region [23,25,26]. Note that the edge of the diffusion region coincides with the edge of the current sheet. Thus, we evaluate Ohm's law at the transition region close to surface 1 as follows:

$$E_y = -V_{z1}B_{xm} \approx -\frac{1}{\Gamma e n'}\partial_j(\mathcal{E}U_y U^j)\big|_1. \tag{A4}$$

At the very edge of the current sheet, the plasma has not yet been accelerated and is essentially in its upstream state, where $\Gamma_1 \approx 1$, $U_{y1} \approx 0$, and the internal energy $\mathcal{E}_1 \approx n'_1 mc^2$. In addition, the $z$-direction derivative dominates, so that $\partial_j(\mathcal{E}U_y U^j) \approx \partial_z(\mathcal{E}U_y U_z)$. Since $U_{y1} \approx 0$, the product rule implies that

$$\partial_z(\mathcal{E}U_y U_z)|_1 = \mathcal{E}U_z(\partial_z U_y)|_1 = \mathcal{E}\Gamma V_z(\partial_z U_y)|_1. \tag{A5}$$

With $U_{z1} = \Gamma_1 V_{z1}$, we can rewrite Eq. (A4) as

$$B_{xm} \approx \frac{mc^2}{e}(\partial_z U_y)|_1. \tag{A6}$$

At the transition region, $U_y$ is very small but has begun to increase toward its peak value at the center of the current sheet. Hence, $(\partial_z U_y)|_1 \approx -U_{y3}/\delta = J_{y3}/2en'_3\delta$.

Finally, use Ampère's law $B_{xm}/4\pi\delta = J_{y3}$ to conclude that the current sheet width is given by the pair plasma inertial length evaluated inside the current sheet:

$$\delta \approx \sqrt{\frac{mc^2}{8\pi n'_3 e^2}}. \tag{A7}$$

*Appendix B: The simulation details.*—Simulations are performed with VPIC, which evolves particles with the relativistic Vlasov equation and fields with Maxwell's equations [37]. We test initial asymptotic magnetizations of $\sigma_{0,\mathrm{init}} = 10$, 100, 500, and 1000. All runs have $x \times z$ system size $1086d_e \times 1086d_e$ and grid size $6144 \times 6144$, except for the $\sigma_{0,\mathrm{init}} = 1000$ run which has grid size $6144 \times 12288$. The initial configuration is a symmetric force-free current sheet without background guide field. The field profile is $\mathbf{B}_0 = B_{x0}[\tanh(z/\lambda)\hat{\mathbf{x}} + \mathrm{sech}(z/\lambda)\hat{\mathbf{y}}]$. The initial current sheet half-width $\lambda = 0.85\sqrt{\sigma_{0,\mathrm{init}}}d_e$, where $d_e \equiv (mc^2/8\pi n_0 e^2)^{1/2}$ is the upstream pair plasma inertial length. Reconnection is initiated with a small magnetic perturbation. Both species have initial temperature $T_0 = 0.5mc^2$, and there are around $7.5 \times 10^9$ macroparticles.


[1] D. Kagan, L. Sironi, B. Cerutti, and D. Giannios, Relativistic magnetic reconnection in pair plasmas and its astrophysical applications, Space Sci. Rev. **191**, 545 (2015).

[2] L. Sironi, M. Petropoulou, and D. Giannios, Relativistic jets shine through shocks or magnetic reconnection?, Mon. Not. R. Astron. Soc. **450**, 183 (2015).

[3] B. Ripperda, M. Liska, K. Chatterjee, G. Musoke, A. A. Philippov, S. B. Markoff, A. Tchekhovskoy, and Z. Younsi, Black hole flares: Ejection of accreted magnetic flux through 3D plasmoid-mediated reconnection, Astrophys. J. Lett. **924**, L32 (2022).

[4] A. Bransgrove, B. Ripperda, and A. Philippov, Magnetic Hair and Reconnection in Black Hole Magnetospheres, Phys. Rev. Lett. **127**, 055101 (2021).

[5] T. di Matteo, Magnetic reconnection: Flares and coronal heating in active galactic nuclei, Mon. Not. R. Astron. Soc. **299**, L15 (1998).

[6] B. Cerutti, G. R. Werner, D. A. Uzdensky, and M. C. Begelman, Gamma-ray flares in the Crab Nebula: A case of relativistic reconnection?, Phys. Plasmas **21**, 056501 (2014).

[7] M. Lyutikov, S. Komissarov, L. Sironi, and O. Porth, Particle acceleration in explosive relativistic reconnection events and Crab Nebula gamma-ray flares, J. Plasma Phys. **84**, 635840201 (2018).

[8] O. Porth, S. S. Komissarov, and R. Keppens, Solution to the sigma problem of pulsar wind nebulae, Mon. Not. R. Astron. Soc. **431**, L48 (2013).

[9] Benoît Cerutti, Alexander A. Philippov, and Guillaume Dubus, Dissipation of the striped pulsar wind and non-thermal particle acceleration: 3D PIC simulations, Astron. Astrophys. **642**, A204 (2020).

[10] Y. Masada, S. Nagataki, K. Shibata, and T. Terasawa, Solar-type magnetic reconnection model for magnetar giant flares, Publ. Astron. Soc. Jpn. **62**, 1093 (2010).

[11] B. Cerutti, D. A. Uzdensky, and M. C. Begelman, Extreme particle acceleration in magnetic reconnection layers: Application to the gamma-ray flares in the Crab Nebula, Astrophys. J. **746**, 148 (2012).

[12] J. F. C. Wardle, D. C. Homan, R. Ojha, and D. H. Roberts, Electron-positron jets associated with the quasar 3C279, Nature (London) **395**, 457 (1998).

[13] B. Crinquand, B. Cerutti, A. Philippov, K. Parfrey, and G. Dubus, Multidimensional Simulations of Ergospheric Pair Discharges around Black Holes, Phys. Rev. Lett. **124**, 145101 (2020).

[14] K. Nalewajko, D. Giannios, M. C. Begelman, D. A. Uzdensky, and M. Sikora, Radiative properties of reconnection-powered minijets in blazars, Mon. Not. R. Astron. Soc. **413**, 333 (2011).

[15] F. Guo, Y.-H. Liu, X. Li, H. Li, W. Daughton, and P. Kilian, Recent progress on particle acceleration and reconnection physics during magnetic reconnection in the magnetically-dominated relativistic regime, Phys. Plasmas **27**, 080501 (2020).

[16] F. Guo, H. Li, W. Daughton, and Y.-H. Liu, Formation of Hard Power Laws in the Energetic Particle Spectra Resulting from Relativistic Magnetic Reconnection, Phys. Rev. Lett. **113**, 155005 (2014).

[17] L. Sironi and A. Spitkovsky, Relativistic reconnection: An efficient source of non-thermal particles, Astrophys. J. **783**, L21 (2014).
[18] D. A. Uzdensky, Relativistic non-thermal particle acceleration in two-dimensional collisionless magnetic reconnection, J. Plasma Phys. **88**, 905880114 (2022).
[19] Y.-H. Liu, P. Cassak, X. Li, M. Hesse, S.-C. Lin, and K. Genestreti, First-principles theory of the rate of magnetic reconnection in magnetospheric and solar plasmas, Commun. Phys. **5**, 97 (2022).
[20] Y.-H. Liu, M. Hesse, F. Guo, W. Daughton, H. Li, P. A. Cassak, and M. A. Shay, Why Does Steady-State Magnetic Reconnection Have a Maximum Local Rate of Order 0.1?, Phys. Rev. Lett. **118**, 085101 (2017).
[21] Y.-H. Liu, S.-C. Lin, M. Hesse, F. Guo, X. Li, H. Zhang, and S. Peery, The critical role of collisionless plasma energization on the structure of relativistic magnetic reconnection, Astrophys. J. **892**, L13 (2020).
[22] G. R. Werner, D. A. Uzdensky, M. C. Begelman, B. Cerutti, and K. Nalewajko, Non-thermal particle acceleration in collisionless relativistic electron-proton reconnection, Mon. Not. R. Astron. Soc. **473**, 4840 (2018).
[23] S. Zenitani, Dissipation in relativistic pair-plasma reconnection: Revisited, Plasma Phys. Controlled Fusion **60**, 014028 (2018).
[24] C. Eckart, The thermodynamics of irreversible processes. III. Relativistic theory of the simple fluid, Phys. Rev. **58**, 919 (1940).
[25] M. Hesse and S. Zenitani, Dissipation in relativistic pair-plasma reconnection, Phys. Plasmas **14**, 112102 (2007).
[26] Q. Y. Xiong, S. Y. Huang, M. Zhou, Z. G. Yuan, X. H. Deng, K. Jiang, Y. Y. Wei, S. B. Xu, J. Zhang, R. T. Lin, and L. Yu, Distribution of negative $J \cdot E'$ in the inflow edge of the inner electron diffusion region during tail magnetic reconnection: Simulations vs observations, Geophys. Res. Lett. **49**, e2022GL098445 (2022).
[27] R. Treumann, R. Nakamura, and W. Baumjohann, Relativistic transformation of phase-space distributions, in *Annales Geophysicae* (Copernicus GmbH, Göttingen, 2011), Vol. 29, pp. 1259–1265.
[28] X. Li and Y.-H. Liu, The effect of thermal pressure on collisionless magnetic reconnection rate, Astrophys. J. **912**, 152 (2021).
[29] J. Birn, M. Hesse, K. Schindler, and S. Zaharia, Role of entropy in magnetotail dynamics, J. Geophys. Res. **114** (2009).
[30] P. Montag, J. Egedal, E. Lichko, and B. Wetherton, Impact of compressibility and a guide field on fermi acceleration during magnetic island coalescence, Phys. Plasmas **24**, 062906 (2017).
[31] Y.-H. Liu, F. Guo, W. Daughton, H. Li, and M. Hesse, Scaling of Magnetic Reconnection in Relativistic Collisionless Pair Plasmas, Phys. Rev. Lett. **114**, 095002 (2015).
[32] B. Ripperda, O. Porth, L. Sironi, and R. Keppens, Relativistic resistive magnetohydrodynamic reconnection and plasmoid formation in merging flux tubes, Mon. Not. R. Astron. Soc. **485**, 299 (2019).
[33] S. D. Yang, Relativistic plasmoid instability in pair plasmas, Astrophys. J. **882**, 105 (2019).
[34] A. Lazarian, G. L. Eyink, A. Jafari, G. Kowal, H. Li, S. Xu, and E. T. Vishniac, 3D turbulent reconnection: Theory, tests, and astrophysical implications, Phys. Plasmas **27**, 012305 (2020).
[35] F. Guo, X. Li, W. Daughton, H. Li, P. Kilian, Y.-H. Liu, Q. Zhang, and H. Zhang, Magnetic energy release, plasma dynamics, and particle acceleration in relativistic turbulent magnetic reconnection, Astrophys. J. **919**, 111 (2021).
[36] C. C. Haggerty, T. N. Parashar, W. H. Matthaeus, M. A. Shay, Y. Yang, M. Wan, P. Wu, and S. Servidio, Exploring the statistics of magnetic reconnection X-points in kinetic particle-in-cell turbulence, Phys. Plasmas **24**, 102308 (2017).
[37] K. J. Bowers, B. J. Albright, L. Yin, B. Bergen, and T. J. T. Kwan, Ultrahigh performance three-dimensional electromagnetic relativistic kinetic plasma simulation, Phys. Plasmas **15**, 055703 (2008).